Quantum Christoffel Nonlinear Magnetization

Xiao-Bin Qiang,[1,*] Xiaoxiong Liu,[1,*] Hai-Zhou Lu,[1,2,†] and X. C. Xie[3,4,5]
[1]State Key Laboratory of Quantum Functional Materials, Department of Physics, and Guangdong Basic Research Center of Excellence for Quantum Science, Southern University of Science and Technology (SUSTech), Shenzhen 518055, China
[2]Quantum Science Center of Guangdong-Hong Kong-Macao Greater Bay Area (Guangdong), Shenzhen 518045, China
[3]International Center for Quantum Materials, School of Physics, Peking University, Beijing 100871, China
[4]Interdisciplinary Center for Theoretical Physics and Information Sciences (ICTPIS), Fudan University, Shanghai 200433, China
[5]Hefei National Laboratory, Hefei 230088, China

(Received 31 July 2025; accepted 13 January 2026; published 3 February 2026)

The Christoffel symbol is an essential quantity in Einstein's general theory of relativity. We discover that an electric field can induce a nonlinear magnetization in quantum materials, described by a Christoffel symbol defined in the Hilbert space of quantum states (quantum Christoffel symbol). Quite different from the previous scenarios, this orbital magnetization does not need spin-orbit coupling and inversion symmetry breaking. Through symmetry analysis and first-principles calculations, we identify a number of point groups and 2D material candidates (e.g., BiF_3, ZnI_2, and Ru_4Se_5) that host this quantum Christoffel nonlinear magnetization. More importantly, this nonlinear magnetization allows the quantum Christoffel symbol to be probed by optical techniques such as magneto-optical Kerr spectroscopy or transport measurements such as tunneling magnetoresistance. This quantum Christoffel nonlinear magnetization gives a paradigm of how geometry dictates physics.

DOI: 10.1103/4kmy-59l9

Introduction—The Christoffel symbol defines how the basis vectors transform in the curved spacetime of Einstein's general theory of relativity (Fig. 1), giving the essential geometric description of gravity [1,2]. The geometry is also tied to a number of nontrivial phenomena in quantum materials [3–10]. In particular, Berry curvature and quantum metric, as the imaginary and real parts of the quantum geometric tensor, have been found playing critical roles in the quantum anomalous Hall effect [11–16], nonlinear transport [17–33], flat-band superconductivity [34–38], and fractional Chern insulators [39–41]. On the other hand, the modern theory of magnetization reveals that the essential role of the rotation of wavepackets [42–49]. The seminal works have demonstrated that the orbital contribution can give rise to linear magnetization in crystalline solids without spin-orbit coupling and in the absence of inversion symmetry [50–56]. These advances have revealed that orbital magnetization is intimately related to the Berry curvature, thereby providing a geometric perspective on the microscopic origin of magnetization. However, in inversion symmetry broken systems, it is challenging to intrinsically distinguish the spin and orbital contributions in experiments because of spin-orbit coupling.

In this Letter, we discover a nonlinear orbital magnetization in quantum materials, described by a quantum version of the Christoffel symbol of the first kind. As

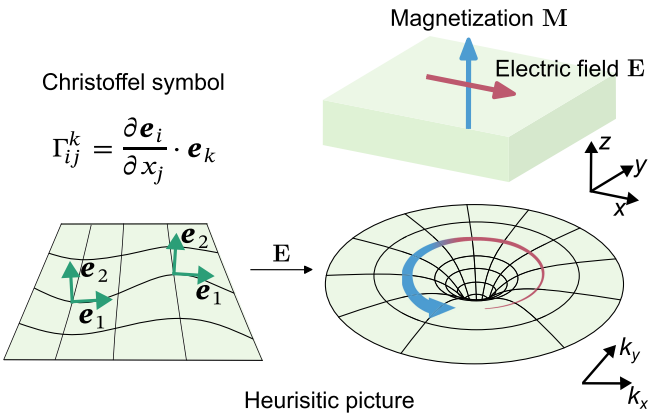

FIG. 1. In Einstein's general relativity, the Christoffel symbol Γ_{ij}^{k} describes how basis vectors $\boldsymbol{e}_i$ transform across the coordinates $\boldsymbol{x}$ of the curved spacetime. We find a nonlinear magnetization $\mathbf{M}$ in response to an electric field $\mathbf{E}$ can be described by a quantum Christoffel symbol $\boldsymbol{\Gamma}$ in momentum space $(k_x - k_y)$, in terms of $\mathbf{M} \propto \mathbf{E}\mathbf{E} \int \boldsymbol{\Gamma}$. A heuristic picture is as follows. One role of the electric field $\mathbf{E}$ is to induce a curved quantum space, described by $\boldsymbol{\Gamma}$. The other role of $\mathbf{E}$ is to drive a "loop current" of electron orbital motion in the curved quantum space, leading to the magnetization $\mathbf{M}$ that is quadratic in $\mathbf{E}$.

*These authors contributed equally to this work.
†Contact author: luhz@sustech.edu.cn

shown in Fig. 1, this orbital magnetization $\mathbf{M}$ is a quadratic nonlinear response to an electric field $\mathbf{E}$. We find that the quantum Christoffel symbol plays an indispensable role in the quadratic relation between $\mathbf{M}$ and $\mathbf{E}$, even dictates for Dirac fermions with particle-hole symmetry [see Eqs. (2) and (3)]. Quite different from the previous scenarios [50–53,57–61], this quantum Christoffel nonlinear magnetization can survive in absence of the spin-orbit coupling in nonmagnetic materials, and does not require inversion symmetry breaking. Through symmetry analysis, we find that the quantum Christoffel nonlinear magnetization can be allowed by many point-group symmetries and hosted by a number of 2D candidate materials. As an example, we use first-principles calculations to evaluate the nonlinear magnetization coefficient for the material BiF_3 and find that the quantum Christoffel nonlinear magnetization is the main contribution in it. Moreover, our calculations indicate that this quantum Christoffel nonlinear magnetization gives rise to a measurable Kerr signal and can be probed via magneto-optical Kerr spectroscopy [62,63]. It may also explain the observed anomalous second-order tunneling magnetoresistance [64].

Quantum Christoffel nonlinear magnetization—To drive the nonlinear magnetization coefficient α_{ijk} defined as $M_i = \alpha_{ijk} E_j E_k$ $(i, j, k \in \{x, y, z\})$, we calculate the quadratic nonlinear orbital magnetization $\mathbf{M}$ induced by an electric field $\mathbf{E}$ (details in Secs. SI–SIII of Supplemental Material [65]). Suppose the quantum state $|\nu\mathbf{k}\rangle$ in a crystal is described by the energy band index ν and wave vector $\mathbf{k}$, the orbital magnetization is the summation of the orbital magnetic moment $\tilde{\mathbf{m}}_\nu(\mathbf{k})$ weighted by the nonequilibrium distribution function $f_\nu(\mathbf{k})$, as

$$\mathbf{M} = \frac{1}{\mathcal{V}} \sum_{\nu,\mathbf{k}} \tilde{\mathbf{m}}_\nu(\mathbf{k}) f_\nu(\mathbf{k}), \tag{1}$$

where $\mathcal{V}$ is volume. Both $\tilde{\mathbf{m}}_\nu(\mathbf{k})$ and $f_\nu(\mathbf{k})$ are modified to include nonequilibrium components induced by the driving electric field $\mathbf{E}$.

In our treatment, $f_\nu(\mathbf{k})$ is derived from the Boltzmann equation [66,70,71] and $\tilde{\mathbf{m}}_\nu(\mathbf{k})$ is evaluated by applying the wave packet dynamics up to the leading order of $\mathbf{E}$ [17,72–74]. Unless necessary, we suppress $\mathbf{k}$ for simplicity.

We find that, for 2D Dirac fermions with particle-hole symmetry, that is, the conduction (c) and valence (v) band energies have the relation $\varepsilon_c(\mathbf{k}) = -\varepsilon_v(\mathbf{k})$, the nonlinear magnetization coefficient

$$\alpha_{ijk} = -\frac{e^3}{2\hbar} \frac{\tau}{\mathcal{V}} \sum_{\nu,\mathbf{k}} \epsilon_{ilr} \Gamma_\nu^{rlj} v_\nu^k f_0', \tag{2}$$

where $i, j, k, l, r \in \{x, y, z\}$ with Einstein summation convention implied over repeated indices, $-e$ is the electron charge, τ is the relaxation time, ϵ_{ilr} is the Levi-Civita antisymmetric tensor, $\boldsymbol{v}_\nu = \nabla_{\mathbf{k}} \varepsilon_\nu(\mathbf{k})/\hbar$ is the intraband velocity, $\varepsilon_\nu(\mathbf{k})$ is the eigen energy for a state with wave vector $\mathbf{k}$ on band ν, and the Fermi-Dirac function $f_0 = [e^{(\varepsilon_\nu - \varepsilon_F)/k_B T} + 1]^{-1}$, with Fermi energy ε_F, Boltzmann constant k_B, and temperature T. Here, f_0' is the derivative of f_0 with respect to ε_ν, so α_{ijk} is primarily contributed by the states near the Fermi surface. More importantly, α_{ijk} explicitly contains a quantum Christoffel symbol

$$\Gamma_\nu^{rlj} = \frac{1}{2} (\partial_j g_\nu^{lr} + \partial_l g_\nu^{rj} - \partial_r g_\nu^{lj}), \tag{3}$$

where ∂_j represents $\partial/(\partial k_j)$, and $\mathbf{g}_\nu = \mathrm{Re} \sum_{\mu \neq \nu} \boldsymbol{\mathcal{A}}_{\nu\mu} \boldsymbol{\mathcal{A}}_{\mu\nu}$ is the quantum metric tensor [3,7–10] defined by the interband Berry connection $\boldsymbol{\mathcal{A}}_{\mu\nu} = i \langle \mu | \nabla_{\mathbf{k}} | \nu \rangle$ [4]. The Christoffel symbol originally characterizes the curved spacetime in Einstein's general relativity through the geodesic equation [1,2] (Appendix A)

$$\ddot{x}_k + \Gamma_{ij}^k \dot{x}_i \dot{x}_j = 0, \tag{4}$$

where $\ddot{x}_k$ and $\dot{x}_{i,j}$ are the derivatives of the coordinates x_i with respect to proper time. In our context, the quantum Christoffel symbol is defined in the Hilbert space of quantum states, and the electric field and magnetization have the analogies

$$E_i \sim \dot{x}_i, \qquad M_k \sim \ddot{x}_k. \tag{5}$$

Recently, the quantum Christoffel symbol has also been introduced to describe momentum-space gravity [75–77].

We now clarify how the quantum Christoffel symbol mediates the quadratic relationship between the orbital magnetization and the electric field. The quantum metric tensor $\mathbf{g}_\nu$ measures the distance between quantum states, thus dictates the trajectory of a moving electron. We now give a hand-waving argument on how the quantum Christoffel symbol gives rise to magnetization. Equation (3) implies that the Einstein summation of the Levi-Civita tensor ϵ_{ilr} with the quantum Christoffel symbol Γ_ν^{rlj} in Eq. (2) can be interpreted as the curl of the quantum metric tensor, i.e., $\epsilon_{ilr} \Gamma_\nu^{rlj} = (\nabla_{\mathbf{k}} \times \mathbf{g}_\nu)^{ij}$. This induces an effective loop current under an applied electric field, giving rise to an orbital magnetization. Moreover, one of the roles of the electric field is to induce the curl of the quantum metric tensor, and the other is to drive the orbital rotation in the curved space of quantum states, so this magnetization is quadratic in the electric field.

Particle-hole symmetry and dominance of the quantum Christoffel symbol—Why particle-hole symmetry guarantees the dominance of the quantum Christoffel symbol in the nonlinear orbital magnetization of Dirac fermions can be understood as follows. Dirac fermions can generically describe a number of semiconductors or insulators with or without topological properties [78]. The Hamiltonian of 2D Dirac fermions can generally be written as $\mathcal{H} = d_0 + \mathbf{d} \cdot \boldsymbol{\sigma}$,

where d_0 and $\mathbf{d} = (d_x, d_y, d_z)$ are functions of the wave vector $\mathbf{k}$, and $\boldsymbol{\sigma} = (\sigma_x, \sigma_y, \sigma_z)$ is the vector of Pauli matrices. In a general case that particle-hole symmetry is not necessary, the nonlinear magnetization coefficient α_{ijk} is found to take the form

$$\alpha_{ijk} = \frac{\tau e^2}{\mathcal{V}} \sum_{\nu,\mathbf{k}} F_\nu^{ij} v_\nu^k f_0', \tag{6}$$

where the magnetoelectric tensor $\mathbf{F}_\nu$ is a band geometric quantity, given by

$$F_\nu^{ij} = -2\mathrm{Re} \sum_{\mu \neq \nu} \frac{m_{\nu\mu}^i \mathcal{A}_{\mu\nu}^j}{\varepsilon_\nu - \varepsilon_\mu} - \frac{e}{2\hbar} \epsilon_{ilr} \Gamma_\nu^{rlj}. \tag{7}$$

Here, $\mathbf{m}_{\mu\nu} = e \sum_{\rho \neq \nu} (\boldsymbol{v}_{\mu\rho} + \delta_{\rho\mu} \boldsymbol{v}_\nu) \times \boldsymbol{\mathcal{A}}_{\rho\nu}/2$ is the interband orbital magnetic moment [17,67], where $\boldsymbol{v}_{\mu\nu} = \langle \mu | \nabla_{\mathbf{k}} \mathcal{H} | \nu \rangle / \hbar$ is the interband velocity. For the Hamiltonian of Dirac fermions, we find that (Sec. SIV of [65]),

$$F_\pm^{ij} = \mp \frac{e}{\hbar} \epsilon_{ikl} \frac{\partial_k d_0}{d} g_\pm^{lj} - \frac{e}{2\hbar} \epsilon_{ilr} \Gamma_\pm^{rlj}, \tag{8}$$

where $d = |\mathbf{d}|$, and $+/-$ correspond to the conduction and valence bands, respectively. In the presence of particle-hole symmetry, $d_0 = 0$, then the first term of $F_\pm^{ij}$ vanishes and only the quantum Christoffel symbol contributes to the nonlinear orbital magnetization.

Symmetry analysis and 2D material candidates—Nonzero components of α_{ijk} can be determined for all crystallographic point group operations, following the general tensor transformation rule. Under an arbitrary symmetry operation represented by the matrix $\mathcal{O}$, the rank-3 tensor α_{ijk} transforms according to $\alpha_{i'j'k'} = \mathrm{Det}(\mathcal{O}) \mathcal{O}_{i'i} \mathcal{O}_{j'j} \mathcal{O}_{k'k} \alpha_{ijk}$, where the determinant factor $\mathrm{Det}(\mathcal{O})$ accounts for the axial nature of α_{ijk}. The symmetry constraints on α_{ijk} for all crystallographic point group operations are summarized in Table I. Specifically, we consider a convenient scenario, α_{zxx}, i.e., the quantum Christoffel nonlinear magnetization polarized along the z direction induced by an x-direction electric field. This response is particularly relevant in experimental settings. For example, under the mirror reflection $\mathcal{M}_x$, the z component of magnetization M_z changes sign ($M_z \to -M_z$), while E_x^2 remains invariant. As a result, the mirror symmetry $\mathcal{M}_x$ forbids a nonzero α_{zxx}. Furthermore, according to the last row of Table I, α_{zxx} is also forbidden by the $\mathcal{C}_{x,y}^2$ and $\mathcal{M}_{x,y}$ symmetries. Therefore, these symmetries must be broken to allow a finite quantum Christoffel nonlinear magnetization, as further illustrated by the model study in Appendix B.

The symmetry analysis presented in Table I indicates that the quantum Christoffel nonlinear magnetization polarized along the z direction is allowed only in materials classified in the point groups 1, $\bar{1}$, 4, $\bar{4}$, 4/m, 3, $\bar{3}$, 6, $\bar{6}$, and 6/m. Based on these symmetry criteria, we utilize the 2DMatPedia database [68] to identify a set of 2D materials that support the quantum nonlinear Christoffel magnetization, as listed in Table II. Among them, the candidates with point group symmetries 4/m, $\bar{3}$, and 6/m simultaneously exhibit inversion and time-reversal symmetries, while the others retain only time-reversal symmetry.

TABLE I. Symmetry constraints of the nonlinear magnetization coefficient α_{ijk} for all point-group symmetry operations. $\mathcal{C}_i^n$ denotes the n-fold rotation ($n = 2, 3, 4, 6$) with respect to the Cartesian axis along the i direction, and $\mathcal{M}_i$ represents a mirror with respect to the plane normal to the i-direction. Symbols ✓ and ✗ mean symmetry-allowed and symmetry-forbidden, respectively. The improper rotations (not listed here) can be derived through $\mathcal{S}_i^n = \mathcal{C}_i^n \mathcal{M}_i$.

	$\mathcal{C}_z^2$	$\mathcal{C}_z^3$	$\mathcal{C}_z^{4,6}$	$\mathcal{C}_x^{2,4,6}$	$\mathcal{C}_y^{2,4,6}$	$\mathcal{C}_x^3$	$\mathcal{C}_y^3$	$\mathcal{M}_z$	$\mathcal{M}_x$	$\mathcal{M}_y$
α_{xxx}	✗	✓	✗	✓	✗	✓	✓	✗	✓	✗
α_{zzz}	✓	✓	✓	✗	✗	✓	✓	✓	✗	✗
α_{xyy}	✗	✓	✗	✓	✗	✓	✗	✗	✓	✗
α_{zxx}	✓	✓	✓	✗	✗	✗	✓	✓	✗	✗

BiF_3 and experimental implementation—To verify the result of the symmetry analysis, we perform first-principles calculations for one of the candidates BiF_3, as an example (technical details in Appendix C). It has a trigonal lattice (space group P$\bar{3}$), as shown in Fig. 2(a). Although BiF_3 contains the heavy element Bi with strong spin-orbit coupling, the electronic states near the Fermi level are dominated by the p orbitals of the F atoms. As a result, the effective spin-orbit coupling near the Fermi level is minimal, as shown by the band structure in Fig. 2(b). By using Eq. (6) and the Wannier interpolation method, we calculate the nonlinear magnetization coefficient α_{zxx} as a function of the Fermi energy ε_F, in the presence and absence of spin-orbit coupling. The two cases yield nearly identical results, as shown in Fig. 2(c), indicating that the nonlinear magnetization is mainly from orbitals and can occur in systems with weak spin-orbit coupling. The spin contribution [61] to the nonlinear magnetization is found to be two orders of magnitude smaller than the orbital contribution in BiF_3 (Sec. SVI of [65]). More importantly, by comparing Eqs. (2) and (6), Fig. 2(d) shows that α_{zxx} can be contributed almost entirely by the quantum Christoffel symbol in BiF_3.

Moreover, due to the $\mathcal{C}_z^3$ symmetry of BiF_3, the magnetization coefficient exhibits the properties $\alpha_{zxx} = \alpha_{zyy}$ and $\alpha_{zxy} = -\alpha_{zyx}$. This symmetry endows an isotropic characteristic,

$$M_z = \alpha_{zxx} |\mathbf{E}|^2, \tag{9}$$

TABLE II. 2D material candidates that could host α_{zxx}, the second-order quantum Christoffel nonlinear magnetization polarized along the z direction induced by an x-direction electric field, based on a search in the open computational database 2DMatPedia [68] of 2D materials as well as verification by the first-principles calculations. The point groups 1 and $\bar{1}$ are discarded. More 2D material candidates that respect the symmetry can be found in Table S2 of [65].

Point group	Candidates
4	$TiPb_9O_{11}$
$\bar{4}$	$Sn_3(HO_2)_2$, $AgBrO_4$
$4/m$	Ru_4Se_5, VPO_5
3	$LiSnCl_3$, $CuBi(PSe_3)_2$
$\bar{3}$	BiF_3, ZnI_2
6	...
$\bar{6}$	$AgNO_3$, $Ge_3Sb_2O_9$
$6/m$	...

which means the magnitude of the induced z-polarized nonlinear magnetization remains invariant with respect to the direction of the in-plane electric field. Remarkably, due to the $\mathcal{C}_z^{n\geq 3}$ symmetry, this isotropic behavior emerges universally among the candidates listed in Table II, which is particularly advantageous for experimental implementation.

The quantum Christoffel nonlinear magnetization can be detected by using the magneto-optical Kerr effect, wherein the polarization state of light reflected from a material is altered by magnetization. The angle between the major axis of the incident linearly polarized light and the major axis of the reflected elliptically polarized light is the Kerr rotation angle θ_K. It can be simulated from the first-principles calculations by using the formula [79–81]

$$\theta_K = \mathrm{Re}\frac{\epsilon_{xy}}{(\epsilon_0 - \epsilon_{xx})\sqrt{\epsilon_{xx}/(d\epsilon_0)}}, \tag{10}$$

where ϵ_0 is the vacuum dielectric constant, d is the sample thickness, and ϵ_{xy} and ϵ_{xx} are dielectric functions. In the presence of an external electric field $\mathbf{E}$, ϵ_{xy} can be expanded up to the second order of $\mathbf{E}$, $\epsilon_{xy} = \epsilon_{xy}^{(0)} + \epsilon_{xy}^{(1)}(\propto \mathbf{E}) + \epsilon_{xy}^{(2)}(\propto \mathbf{E}^2) + \cdots$, where the equilibrium dielectric function $\epsilon_{xy}^{(0)}$ and first-order nonequilibrium dielectric function $\epsilon_{xy}^{(1)}$ are forbidden by time-reversal and inversion symmetries, respectively [82]. Therefore, the only nonzero term is $\epsilon_{xy}^{(2)}$. In practice, the dielectric functions are determined by the optical conductivities as $\epsilon_{xx} = \epsilon_0 + i\sigma_{xx}(\omega)/\omega$ and $\epsilon_{xy}^{(2)} = i\sigma_{xy}(\omega)/\omega$, where ω is the light frequency [62,63]. The optical conductivity $\sigma_{ij}(\omega)$ can be calculated by using the Kubo-Greenwood formula [83,84]

$$\sigma_{ij}(\omega) = \frac{e^2\hbar}{i\mathcal{V}}\sum_{\nu,\mu,\mathbf{k}}\frac{f_0(\varepsilon_\nu) - f_0(\varepsilon_\mu)}{\varepsilon_\mu - \varepsilon_\nu}\frac{\langle\nu|v_i|\mu\rangle\langle\mu|v_j|\nu\rangle}{(\varepsilon_\mu - \varepsilon_\nu) - \hbar\omega - i\eta}, \tag{11}$$

where $v_i = \nabla_{k_i}\mathcal{H}/\hbar$ is the velocity operator along the i direction, $\hbar\omega$ is the photon energy, and η is an infinitesimal.

To evaluate the Kerr angle using first-principles calculations, we introduce a Haldane-like perturbation $\mathcal{H}'$ to simulate the effect of magnetization

$$\mathcal{H}' = \sum_{\langle\langle i,j\rangle\rangle}\sum_{a,b} t' e^{i\theta_{ij,ab}} c_{i,a}^\dagger c_{j,b}, \tag{12}$$

where $\langle\langle i, j\rangle\rangle$ denotes the second-nearest sites of Bi atoms, $a, b \in \{p_x, p_y\}$ with $a \neq b$, and only the hoppings between p_x, p_y orbitals of Bi atoms are considered. To maintain the $\mathcal{C}_z^3$ symmetry, the hopping phase factor θ_{ij,p_xp_y} is chosen with respect to the hopping direction, taking values (0, $\pm 2\pi/3$, $\pm 4\pi/3$). Crucially, a $2\pi/3$ difference between θ_{ij,p_xp_y} and θ_{ij,p_yp_x} is needed to break time-reversal symmetry.

As shown in Fig. 2(c), the behavior of α_{zxx} near the Fermi energy can be well described by the Wannier Hamiltonian with the perturbation $\mathcal{H}'$ for a hopping magnitude of $t' = 2$ meV. Moreover, α_{zxx} for the finite hole doping can induce a nonlinear orbital magnetic moment per unit cell of the order of $10^{-4}\mu_B$, if we assume that the BiF_3 sample is in an in-plane electric field of the order of 0.02 V/μm and the relaxation time $\tau = 100$ ps. This ensures that the magnetization can be detected by the magneto-optical Kerr spectroscopy.

Figure 2(e) displays the simulated Kerr rotation angle θ_K as a function of photon energy $\hbar\omega$, calculated by using the perturbed Wannier Hamiltonian for the Fermi energies at −0.25 and −0.10 eV. The predicted Kerr rotation amplitudes are on the order of μrad, which is well above the typical experimental detection limit (on the order of $n$rad [85]). This estimation is based on a relaxation time of $\tau = 100$ ps, and even shorter relaxation times down to the picosecond range can still yield detectable Kerr signals under suitable conditions. In addition, our analysis identifies the 2–3 eV photon energy range as optimal, exhibiting a pronounced Kerr angle θ_K across a broad doping window. Here, the Kerr signal of the nonlinear magnetization in time-reversal-symmetric systems can be distinguished from those of the conventional magneto-optical effects as they vanish identically in the presence of time-reversal symmetry. In particular, the inverse Faraday effect requires circularly polarized light and is inherently tied to mechanisms that break time-reversal symmetry [86–89]. While linearly polarized light can be converted into circular polarization, this conversion unavoidably relies on time-reversal-symmetry breaking.

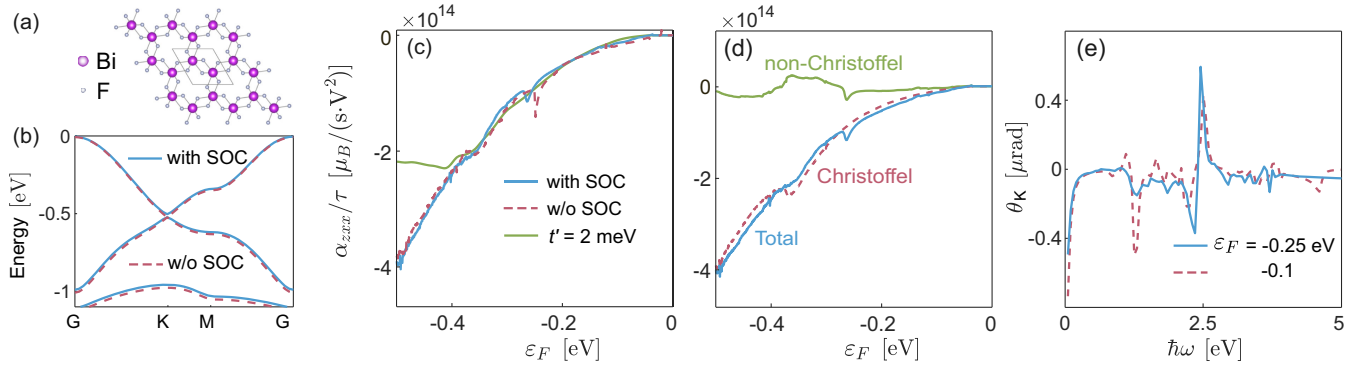

FIG. 2. (a) Lattice structure of the 2D BiF_3 grown along the [001] crystallographic direction. (b) Band structure of the 2D BiF_3 along the high symmetry line with and without spin-orbit coupling (SOC). (c) First-principles calculation results of the nonlinear magnetization coefficient α_{zxx} as a function of the Fermi energy ε_F, by using Eq. (6) (with and without SOC) and also with the Haldane-like perturbation $\mathcal{H}'$ Eq. (12) ($t' = 2$ meV), respectively. In the calculation with $\mathcal{H}'$, the hopping parameter $t' = 2$ meV, relaxation time $\tau = 100$ ps, and additional electric field $\mathbf{E} = 0.02$ V/μm. (d) First-principles calculation results of α_{zxx} as a function of the Fermi energy ε_F, by using Eqs. (2) (Christoffel) and (6) (Total), respectively. The non-Christoffel contribution is much smaller than the contribution described by the quantum Christoffel symbol. (e) Kerr rotation angle θ_K as a function of photon energy $\hbar\omega$, at Fermi levels −0.25 eV and −0.10 eV, respectively. The Kerr angle measures how much a linearly polarized light is rotated after being reflected from the sample and is a direct probe of magnetization.

Thus, the nonlinear magnetization uncovered here is fundamentally distinct from previously known magneto-optical effects and constitutes a genuinely new mechanism.

In the above, we have focused on nonmagnetic materials, thereby eliminating all time-reversal-odd contributions (see Secs. SIII and SV of [65]). Moreover, as a second-order response, α_{ijk} can remain nonzero even in centrosymmetric materials and is fundamentally independent of spin-orbit coupling. This opens new avenues for realizing nonlinear orbitronic phenomena [85,90–97] in light-element materials and high-symmetry systems that were previously considered unsuitable for spin-orbit-driven effects.

Acknowledgments—We thank Xuan Qian, Kaiyou Wang, Yang Ji, Rui Chen, Chunming Wang, Zongzheng Du, Xiangang Wan, and Xiaoqun Wang for the insightful discussions. This work is supported by the National Key R&D Program of China (2022YFA1403700), the National Natural Science Foundation of China (12525401 and 12350402), Quantum Science and Technology—National Science and Technology Major Project (Grant No. 2021ZD0302400), Guangdong Basic and Applied Basic Research Foundation (2023B0303000011), Guangdong Provincial Quantum Science Strategic Initiative (GDZX2201001 and GDZX2401001), the Science, Technology and Innovation Commission of Shenzhen Municipality (ZDSYS20190902092905285), High-level Special Funds (G03050K004), the New Cornerstone Science Foundation through the XPLORER PRIZE, and the Center for Computational Science and Engineering of SUSTech.

Data availability—The data that support the findings of this article are not publicly available. The data are available from the authors upon reasonable request.

[1] C. W. Misner, K. S. Thorne, and J. A. Wheeler, *Gravitation* (Princeton University Press, Princeton, 2017).
[2] R. M. Wald, *General Relativity* (University of Chicago Press, Chicago, 2010).
[3] J. Provost and G. Vallee, Riemannian structure on manifolds of quantum states, Commun. Math. Phys. **76**, 289 (1980).
[4] M. V. Berry, Quantal phase factors accompanying adiabatic changes, Proc. R. Soc. A **392**, 45 (1984).
[5] J. Anandan and Y. Aharonov, Geometry of quantum evolution, Phys. Rev. Lett. **65**, 1697 (1990).
[6] D. Xiao, M.-C. Chang, and Q. Niu, Berry phase effects on electronic properties, Rev. Mod. Phys. **82**, 1959 (2010).
[7] R. Resta, The insulating state of matter: A geometrical theory, Eur. Phys. J. B **79**, 121 (2011).
[8] P. Törmä, Essay: Where can quantum geometry lead us?, Phys. Rev. Lett. **131**, 240001 (2023).
[9] T. Liu, X.-B. Qiang, H.-Z. Lu, and X. C. Xie, Quantum geometry in condensed matter, Natl. Sci. Rev. **12**, nwae334 (2024).
[10] Y. Jiang, T. Holder, and B. Yan, Revealing quantum geometry in nonlinear quantum materials, Rep. Prog. Phys. **88**, 076502 (2025).
[11] F. D. M. Haldane, Model for a quantum Hall effect without Landau levels: Condensed-matter realization of the parity anomaly, Phys. Rev. Lett. **61**, 2015 (1988).
[12] N. Nagaosa, J. Sinova, S. Onoda, A. H. MacDonald, and N. P. Ong, Anomalous Hall effect, Rev. Mod. Phys. **82**, 1539 (2010).

[13] H.-Z. Lu, W.-Y. Shan, W. Yao, Q. Niu, and S.-Q. Shen, Massive Dirac fermions and spin physics in an ultrathin film of topological insulator, Phys. Rev. B **81**, 115407 (2010).
[14] R. Yu, W. Zhang, H.-J. Zhang, S.-C. Zhang, X. Dai, and Z. Fang, Quantized anomalous Hall effect in magnetic topological insulators, Science **329**, 61 (2010).
[15] C.-Z. Chang, J. Zhang, X. Feng, J. Shen, Z. Zhang, M. Guo, K. Li, Y. Ou, P. Wei, L.-L. Wang *et al.*, Experimental observation of the quantum anomalous Hall effect in a magnetic topological insulator, Science **340**, 167 (2013).
[16] C.-Z. Chang, C.-X. Liu, and A. H. MacDonald, Colloquium: Quantum anomalous Hall effect, Rev. Mod. Phys. **95**, 011002 (2023).
[17] Y. Gao, S. A. Yang, and Q. Niu, Field induced positional shift of Bloch electrons and its dynamical implications, Phys. Rev. Lett. **112**, 166601 (2014).
[18] I. Sodemann and L. Fu, Quantum nonlinear Hall effect induced by Berry curvature dipole in time-reversal invariant materials, Phys. Rev. Lett. **115**, 216806 (2015).
[19] Z. Z. Du, C. M. Wang, H.-Z. Lu, and X. C. Xie, Band signatures for strong nonlinear Hall effect in bilayer WTe_2, Phys. Rev. Lett. **121**, 266601 (2018).
[20] Z. Du, H.-Z. Lu, and X. Xie, Nonlinear Hall effects, Nat. Rev. Phys. **3**, 744 (2021).
[21] C. Wang, Y. Gao, and D. Xiao, Intrinsic nonlinear Hall effect in antiferromagnetic tetragonal CuMnAs, Phys. Rev. Lett. **127**, 277201 (2021).
[22] H. Liu, J. Zhao, Y.-X. Huang, W. Wu, X.-L. Sheng, C. Xiao, and S. A. Yang, Intrinsic second-order anomalous Hall effect and its application in compensated antiferromagnets, Phys. Rev. Lett. **127**, 277202 (2021).
[23] Q. Ma, S.-Y. Xu, H. Shen, D. MacNeill, V. Fatemi, T.-R. Chang, A. M. Mier Valdivia, S. Wu, Z. Du, C.-H. Hsu *et al.*, Observation of the nonlinear Hall effect under time-reversal-symmetric conditions, Nature (London) **565**, 337 (2019).
[24] K. Kang, T. Li, E. Sohn, J. Shan, and K. F. Mak, Nonlinear anomalous Hall effect in few-layer WTe_2, Nat. Mater. **18**, 324 (2019).
[25] A. Tiwari, F. Chen, S. Zhong, E. Drueke, J. Koo, A. Kaczmarek, C. Xiao, J. Gao, X. Luo, Q. Niu *et al.*, Giant c-axis nonlinear anomalous Hall effect in Td-$MoTe_2$ and WTe_2, Nat. Commun. **12**, 2049 (2021).
[26] D. Kumar, C.-H. Hsu, R. Sharma, T.-R. Chang, P. Yu, J. Wang, G. Eda, G. Liang, and H. Yang, Room-temperature nonlinear Hall effect and wireless radiofrequency rectification in Weyl semimetal $TaIrTe_4$, Nat. Nanotechnol. **16**, 421 (2021).
[27] T. Ma, H. Chen, K. Yananose, X. Zhou, L. Wang, R. Li, Z. Zhu, Z. Wu, Q.-H. Xu, J. Yu *et al.*, Growth of bilayer $MoTe_2$ single crystals with strong non-linear Hall effect, Nat. Commun. **13**, 5465 (2022).
[28] M. Huang, Z. Wu, J. Hu, X. Cai, E. Li, L. An, X. Feng, Z. Ye, N. Lin, K. T. Law *et al.*, Giant nonlinear Hall effect in twisted bilayer WSe_2, Natl. Sci. Rev. **10**, nwac232 (2023).
[29] A. Gao, Y.-F. Liu, J.-X. Qiu, B. Ghosh, T. V. Trevisan, Y. Onishi, C. Hu, T. Qian, H.-J. Tien, S.-W. Chen *et al.*, Quantum metric nonlinear Hall effect in a topological antiferromagnetic heterostructure, Science **381**, 181 (2023).
[30] N. Wang, D. Kaplan, Z. Zhang, T. Holder, N. Cao, A. Wang, X. Zhou, F. Zhou, Z. Jiang, C. Zhang *et al.*, Quantum-metric-induced nonlinear transport in a topological antiferromagnet, Nature (London) **621**, 487 (2023).
[31] J. Jia, L. Xiang, Z. Qiao, and J. Wang, Equivalence of semiclassical and response theories for second-order nonlinear ac Hall effects, Phys. Rev. B **110**, 245406 (2024).
[32] X.-B. Qiang, T. Liu, Z.-X. Gao, H.-Z. Lu, and X. C. Xie, A clarification on quantum-metric-induced nonlinear transport, Adv. Sci. e14818 (2025).
[33] C. Xiao, J. Cao, Q. Niu, and S. A. Yang, Proper definition of intrinsic nonlinear current, Phys. Rev. Lett. **135**, 256306 (2025).
[34] S. Peotta and P. Törmä, Superfluidity in topologically nontrivial flat bands, Nat. Commun. **6**, 8944 (2015).
[35] A. Julku, S. Peotta, T. I. Vanhala, D.-H. Kim, and P. Törmä, Geometric origin of superfluidity in the Lieb-lattice flat band, Phys. Rev. Lett. **117**, 045303 (2016).
[36] L. Liang, T. I. Vanhala, S. Peotta, T. Siro, A. Harju, and P. Törmä, Band geometry, Berry curvature, and superfluid weight, Phys. Rev. B **95**, 024515 (2017).
[37] P. Törmä, L. Liang, and S. Peotta, Quantum metric and effective mass of a two-body bound state in a flat band, Phys. Rev. B **98**, 220511(R) (2018).
[38] K.-E. Huhtinen, J. Herzog-Arbeitman, A. Chew, B. A. Bernevig, and P. Törmä, Revisiting flat band superconductivity: Dependence on minimal quantum metric and band touchings, Phys. Rev. B **106**, 014518 (2022).
[39] S. A. Parameswaran, R. Roy, and S. L. Sondhi, Fractional Chern insulators and the W_∞ algebra, Phys. Rev. B **85**, 241308(R) (2012).
[40] R. Roy, Band geometry of fractional topological insulators, Phys. Rev. B **90**, 165139 (2014).
[41] T. S. Jackson, G. Möller, and R. Roy, Geometric stability of topological lattice phases, Nat. Commun. **6**, 8629 (2015).
[42] D. Xiao, J. Shi, and Q. Niu, Berry phase correction to electron density of states in solids, Phys. Rev. Lett. **95**, 137204 (2005).
[43] T. Thonhauser, D. Ceresoli, D. Vanderbilt, and R. Resta, Orbital magnetization in periodic insulators, Phys. Rev. Lett. **95**, 137205 (2005).
[44] D. Ceresoli, T. Thonhauser, D. Vanderbilt, and R. Resta, Orbital magnetization in crystalline solids: Multi-band insulators, Chern insulators, and metals, Phys. Rev. B **74**, 024408 (2006).
[45] J. Shi, G. Vignale, D. Xiao, and Q. Niu, Quantum theory of orbital magnetization and its generalization to interacting systems, Phys. Rev. Lett. **99**, 197202 (2007).
[46] F. Aryasetiawan and K. Karlsson, Modern theory of orbital magnetic moment in solids, J. Phys. Chem. Solids **128**, 87 (2019).
[47] L. Dong, C. Xiao, B. Xiong, and Q. Niu, Berry phase effects in dipole density and the Mott relation, Phys. Rev. Lett. **124**, 066601 (2020).
[48] R. Burgos Atencia, A. Agarwal, and D. Culcer, Orbital angular momentum of Bloch electrons: Equilibrium

formulation, magneto-electric phenomena, and the orbital Hall effect, Adv. Phys. **9**, 2371972 (2024).
[49] X.-B. Qiang, T. Liu, H.-Z. Lu, and X. Xie, Quantum geometric origin of orbital magnetization, Appl. Phys. Lett. **128**, 010501, (2026).
[50] T. Yoda, T. Yokoyama, and S. Murakami, Current-induced orbital and spin magnetizations in crystals with helical structure, Sci. Rep. **5**, 12024 (2015).
[51] S. Zhong, J. E. Moore, and I. Souza, Gyrotropic magnetic effect and the magnetic moment on the Fermi surface, Phys. Rev. Lett. **116**, 077201 (2016).
[52] J. Rou, C. Şahin, J. Ma, and D. A. Pesin, Kinetic orbital moments and nonlocal transport in disordered metals with nontrivial band geometry, Phys. Rev. B **96**, 035120 (2017).
[53] D. Hara, M. S. Bahramy, and S. Murakami, Current-induced orbital magnetization in systems without inversion symmetry, Phys. Rev. B **102**, 184404 (2020).
[54] Y. Lee, A. Knothe, H. Overweg, M. Eich, C. Gold, A. Kurzmann, V. Klasovika, T. Taniguchi, K. Wantanabe, V. Fal'ko *et al.*, Tunable valley splitting due to topological orbital magnetic moment in bilayer graphene quantum point contacts, Phys. Rev. Lett. **124**, 126802 (2020).
[55] Z. Ge, S. Slizovskiy, P. Polizogopoulos, T. Joshi, T. Taniguchi, K. Watanabe, D. Lederman, V. I. Fal'ko, and J. Velasco, Jr., Giant orbital magnetic moments and paramagnetic shift in artificial relativistic atoms and molecules, Nat. Nanotechnol. **18**, 250 (2023).
[56] A. Johansson, Theory of spin and orbital Edelstein effects, J. Phys. Condens. Matter **36**, 423002 (2024).
[57] V. Edelstein, Spin polarization of conduction electrons induced by electric current in two-dimensional asymmetric electron systems, Solid State Commun. **73**, 233 (1990).
[58] Y. K. Kato, R. C. Myers, A. C. Gossard, and D. D. Awschalom, Current-induced spin polarization in strained semiconductors, Phys. Rev. Lett. **93**, 176601 (2004).
[59] A. Manchon, J. Železný, I. M. Miron, T. Jungwirth, J. Sinova, A. Thiaville, K. Garello, and P. Gambardella, Current-induced spin-orbit torques in ferromagnetic and antiferromagnetic systems, Rev. Mod. Phys. **91**, 035004 (2019).
[60] C. Xiao, H. Liu, W. Wu, H. Wang, Q. Niu, and S. A. Yang, Intrinsic nonlinear electric spin generation in centrosymmetric magnets, Phys. Rev. Lett. **129**, 086602 (2022).
[61] C. Xiao, W. Wu, H. Wang, Y.-X. Huang, X. Feng, H. Liu, G.-Y. Guo, Q. Niu, and S. A. Yang, Time-reversal-even nonlinear current induced spin polarization, Phys. Rev. Lett. **130**, 166302 (2023).
[62] S. Sugano and N. Kojima, *Magneto-Optics* (Springer Science & Business Media, New York, 2013), Vol. 128.
[63] W. Kuch, R. Schäfer, P. Fischer, and F. U. Hillebrecht, *Magnetic Microscopy of Layered Structures* (Springer, New York, 2015), Vol. 57.
[64] X.-G. Ye, P.-F. Zhu, W.-Z. Xu, T.-Y. Zhao, and Z.-M. Liao, Nonlinear spin and orbital Edelstein effect in WTe_2, Phys. Rev. B **110**, L201407 (2024).
[65] See Supplemental Material at http://link.aps.org/supplemental/10.1103/4kmy-59l9 for (Sec. SI) calculation of orbital magnetic moment correction, (Sec. SII) calculation of distribution function, (Sec. SIII) calculation of nonlinear magnetization coefficient, (Sec. SIV) particle-hole symmetry and solo of quantum Christoffel symbol, (Sec. SV) symmetry analysis and 2D material candidates, and (Sec. SVI) comparison with spin contribution, which includes Refs. [6,17,21,22,66–69].
[66] H. Haug and A.-P. Jauho, *Quantum Kinetics in Transport and Optics of Semiconductors* (Springer, New York, 2008), Vol. 2.
[67] H. Wang, Y.-X. Huang, H. Liu, X. Feng, J. Zhu, W. Wu, C. Xiao, and S. A. Yang, Orbital origin of the intrinsic planar Hall effect, Phys. Rev. Lett. **132**, 056301 (2024).
[68] J. Zhou, L. Shen, M. D. Costa, K. A. Persson, S. P. Ong, P. Huck, Y. Lu, X. Ma, Y. Chen, H. Tang *et al.*, 2DMatPedia, an open computational database of two-dimensional materials from top-down and bottom-up approaches, Sci. Data **6**, 86 (2019).
[69] A. Graf and F. Piéchon, Berry curvature and quantum metric in N-band systems: An eigenprojector approach, Phys. Rev. B **104**, 085114 (2021).
[70] Z. Du, C. Wang, S. Li, H.-Z. Lu, and X. Xie, Disorder-induced nonlinear Hall effect with time-reversal symmetry, Nat. Commun. **10**, 3047 (2019).
[71] X.-B. Qiang, Z. Z. Du, H.-Z. Lu, and X. C. Xie, Topological and disorder corrections to the transverse Wiedemann-Franz law and Mott relation in kagome magnets and Dirac materials, Phys. Rev. B **107**, L161302 (2023).
[72] Y. Gao, S. A. Yang, and Q. Niu, Geometrical effects in orbital magnetic susceptibility, Phys. Rev. B **91**, 214405 (2015).
[73] Y. Gao, Semiclassical dynamics and nonlinear charge current, Front. Phys. **14**, 1 (2019).
[74] C. Xiao, H. Liu, J. Zhao, S. A. Yang, and Q. Niu, Thermoelectric generation of orbital magnetization in metals, Phys. Rev. B **103**, 045401 (2021).
[75] T. B. Smith, L. Pullasseri, and A. Srivastava, Momentum-space gravity from the quantum geometry and entropy of Bloch electrons, Phys. Rev. Res. **4**, 013217 (2022).
[76] M. Mehraeen, Quantum response theory and momentum-space gravity, Phys. Rev. Lett. **135**, 156302 (2025).
[77] Y. Onishi, N. Paul, and L. Fu, Emergent curved space and gravitational lensing in quantum materials, Phys. Rev. B **113**, 024401 (2026).
[78] S.-Q. Shen, *Topological Insulators: Dirac Equation in Condensed Matter* (Springer, New York, 2017), Vol. 187.
[79] W. Feng, G.-Y. Guo, J. Zhou, Y. Yao, and Q. Niu, Large magneto-optical Kerr effect in noncollinear antiferromagnets $Mn_3X(X = Rh, Ir, Pt)$, Phys. Rev. B **92**, 144426 (2015).
[80] G. Y. Guo and H. Ebert, Theoretical investigation of the orientation dependence of the magneto-optical Kerr effect in Co, Phys. Rev. B **50**, 10377 (1994).
[81] G. Y. Guo and H. Ebert, Band-theoretical investigation of the magneto-optical Kerr effect in Fe and Co multilayers, Phys. Rev. B **51**, 12633 (1995).
[82] S. S. Tsirkin, P. A. Puente, and I. Souza, Gyrotropic effects in trigonal tellurium studied from first principles, Phys. Rev. B **97**, 035158 (2018).
[83] R. Kubo, Statistical-mechanical theory of irreversible processes. I. General theory and simple applications to magnetic and conduction problems, J. Phys. Soc. Jpn. **12**, 570 (1957).
[84] D. A. Greenwood, The Boltzmann equation in the theory of electrical conduction in metals, Proc. Phys. Soc. London **71**, 585 (1958).

[85] Y.-G. Choi, D. Jo, K.-H. Ko, D. Go, K.-H. Kim, H. G. Park, C. Kim, B.-C. Min, G.-M. Choi, and H.-W. Lee, Observation of the orbital Hall effect in a light metal Ti, Nature (London) **619**, 52 (2023).
[86] D. Popova, A. Bringer, and S. Blügel, Theory of the inverse Faraday effect in view of ultrafast magnetization experiments, Phys. Rev. B **84**, 214421 (2011).
[87] R. V. Mikhaylovskiy, E. Hendry, and V. V. Kruglyak, Ultrafast inverse Faraday effect in a paramagnetic terbium gallium garnet crystal, Phys. Rev. B **86**, 100405(R) (2012).
[88] M. Battiato, G. Barbalinardo, and P. M. Oppeneer, Quantum theory of the inverse Faraday effect, Phys. Rev. B **89**, 014413 (2014).
[89] T. Dannegger, M. Berritta, K. Carva, S. Selzer, U. Ritzmann, P. M. Oppeneer, and U. Nowak, Ultrafast coherent all-optical switching of an antiferromagnet with the inverse Faraday effect, Phys. Rev. B **104**, L060413 (2021).
[90] B. A. Bernevig, T. L. Hughes, and S.-C. Zhang, Orbitronics: The intrinsic orbital current in p-doped silicon, Phys. Rev. Lett. **95**, 066601 (2005).
[91] T. Tanaka, H. Kontani, M. Naito, T. Naito, D. S. Hirashima, K. Yamada, and J. Inoue, Intrinsic spin Hall effect and orbital Hall effect in $4d$ and $5d$ transition metals, Phys. Rev. B **77**, 165117 (2008).
[92] D. Go, D. Jo, H.-W. Lee, M. Kläui, and Y. Mokrousov, Orbitronics: Orbital currents in solids, Europhys. Lett. **135**, 37001 (2021).
[93] P. Wang, F. Chen, Y. Yang, S. Hu, Y. Li, W. Wang, D. Zhang, and Y. Jiang, Orbitronics: Mechanisms, materials and devices, Adv. Electron. Mater. **11**, 2400554 (2024).
[94] D. Jo, D. Go, G.-M. Choi, and H.-W. Lee, Spintronics meets orbitronics: Emergence of orbital angular momentum in solids, npj Spintron. **2**, 19 (2024).
[95] L. Wang, J. Zhu, H. Chen, H. Wang, J. Liu, Y.-X. Huang, B. Jiang, J. Zhao, H. Shi, G. Tian *et al.*, Orbital magneto-nonlinear anomalous Hall effect in kagome magnet Fe_3Sn_2, Phys. Rev. Lett. **132**, 106601 (2024).
[96] H. Liu and D. Culcer, Dominance of extrinsic scattering mechanisms in the orbital Hall effect: Graphene, transition metal dichalcogenides, and topological antiferromagnets, Phys. Rev. Lett. **132**, 186302 (2024).
[97] H. Liu, J. H. Cullen, D. P. Arovas, and D. Culcer, Quantum correction to the orbital Hall effect, Phys. Rev. Lett. **134**, 036304 (2025).
[98] P. Tang, Q. Zhou, G. Xu, and S.-C. Zhang, Dirac fermions in an antiferromagnetic semimetal, Nat. Phys. **12**, 1100 (2016).
[99] G. Kresse and J. Furthmüller, Efficiency of *ab-initio* total energy calculations for metals and semiconductors using a plane-wave basis set, Comput. Mater. Sci. **6**, 15 (1996).
[100] G. Kresse and D. Joubert, From ultrasoft pseudopotentials to the projector augmented-wave method, Phys. Rev. B **59**, 1758 (1999).
[101] G. Kresse and J. Furthmüller, Efficient iterative schemes for *ab initio* total-energy calculations using a plane-wave basis set, Phys. Rev. B **54**, 11169 (1996).
[102] J. P. Perdew, K. Burke, and M. Ernzerhof, Generalized gradient approximation made simple, Phys. Rev. Lett. **77**, 3865 (1996).
[103] X. Wang, J. R. Yates, I. Souza, and D. Vanderbilt, *Ab initio* calculation of the anomalous Hall conductivity by Wannier interpolation, Phys. Rev. B **74**, 195118 (2006).
[104] S. S. Tsirkin, High performance Wannier interpolation of Berry curvature and related quantities with WannierBerri code, npj Comput. Mater. **7**, 1 (2021).
[105] G. Pizzi, V. Vitale, R. Arita, S. Blügel, F. Freimuth, G. Géranton, M. Gibertini, D. Gresch, C. Johnson, T. Koretsune *et al.*, Wannier90 as a community code: New features and applications, J. Phys. Condens. Matter **32**, 165902 (2020).
[106] O. Jepson and O. Anderson, The electronic structure of h.c.p. ytterbium, Solid State Commun. **9**, 1763 (1971).
[107] M. Methfessel and A. T. Paxton, High-precision sampling for Brillouin-zone integration in metals, Phys. Rev. B **40**, 3616 (1989).

End Matter

Appendix A: Tutorial on Christoffel symbol in Einstein's general relativity—The motion of a free particle in curved spacetime of general theory relativity is governed by the geodesic equation

$$\ddot{x}_k + \Gamma^k_{ij}\dot{x}_i\dot{x}_j = 0, \tag{A1}$$

which generalizes Newton's second law to a curved spacetime, where $\ddot{x}_k$ and $\dot{x}_{i,j}$ denote the derivatives of x_i with respect to proper time. The geometric properties of spacetime are encoded in the affine connection

$$\Gamma^k_{ij} = \frac{\partial \boldsymbol{e}_i}{\partial x_j} \cdot \boldsymbol{e}_k, \tag{A2}$$

which characterizes the variation of the basis vectors $\boldsymbol{e}_i$'s throughout a given coordinate system (Fig. 1), where $i, j, k \in \{x_0, x_1, x_2, x_3\}$, the superscripts denote contravariant components, while the subscripts denote covariant components. The spacetime in Einstein's general theory of relativity is a torsion-free manifold. Consequently, the affine connection Γ^k_{ij} is symmetric and is entirely determined by the metric tensor as [1,2]

$$\Gamma^k_{ij} = \frac{1}{2} g^{kl}(\partial_i g_{lj} + \partial_j g_{li} - \partial_l g_{ij}), \tag{A3}$$

known as the Christoffel symbol of the second kind, where ∂_i represents $\partial/(\partial x_i)$, and g_{lj} and g^{kl} denote the covariant and contravariant metric tensor, respectively.

Additionally, the Christoffel symbol of the first kind is defined by

$$\Gamma_{lij} = g_{lk}\Gamma^k_{ij} = \frac{1}{2}(\partial_i g_{lj} + \partial_j g_{li} - \partial_l g_{ij}), \tag{A4}$$

where all components are covariant. In quantum geometry, all quantities are typically treated as covariant. Since an additional band index ν is required, we will henceforth denote Γ_ν^{lij} [Eq. (3)] as the quantum Christoffel symbol.

Appendix B: Minimal model for quantum Christoffel nonlinear magnetization—To have an intuitive picture of when the quantum Christoffel nonlinear magnetization can emerge, we perform calculations of the nonlinear magnetization coefficient α_{zxx} for a four-band massive Dirac model [78,98],

$$\mathcal{H} = v(k_x\tau_x\sigma_x + k_y\tau_x\sigma_y) + m\tau_z + tk_xk_y\tau_z + \lambda k^2, \tag{B1}$$

where v, m, t, and λ are model parameters, and τ_i's and σ_i's denote two sets of Pauli matrices. The term $tk_xk_y\tau_z$ is included to break $\mathcal{C}_{x,y}^2$ (twofold rotations about the x and y axes) and $\mathcal{M}_{x,y}$ (mirror reflections with respect to the planes normal to the x and y directions) symmetries, which is necessary for a nonzero α_{zxx}, as illustrated in Table I. Moreover, the last term λk^2 is introduced to break the particle-hole symmetry. Insets in Figs. 3(a) and 3(c) compare the band structures without and with particle-hole symmetry, respectively. When $\lambda \neq 0$, the nonlinear magnetization coefficient is determined by Eq. (6). Figure 3(a) compares α_{zxx} from the quantum Christoffel nonlinear magnetization and non-Christoffel contribution in absence of particle-hole symmetry. Over the entire range of Fermi energy, the Christoffel contribution is dominant. As shown in Fig. 3(b), with increasing λ, that is, stronger violation of particle-hole symmetry, non-Christoffel contribution increases, although Christoffel contribution remains dominant.

For the particle-hole symmetric case ($\lambda = 0$), the nonlinear magnetization is solely governed by the quantum Christoffel symbol Γ_ν^{ijk}, and α_{zxx} takes the form

$$\alpha_{zxx} = \frac{\tau e^3}{2\hbar\mathcal{V}} \sum_{\nu,\mathbf{k}} v_\nu^x f_0'(\Gamma_\nu^{xyx} - \Gamma_\nu^{yxx}). \tag{B2}$$

Figure 3(c) shows α_{zxx} as a function of the Fermi energy ε_F for different values of t. The magnitude of α_{zxx} becomes pronounced near the band edge, where the quantum geometric contribution is significantly enhanced. Furthermore, as shown in Fig. 3(d), a nonzero t is essential for breaking the relevant symmetries and enabling a finite α_{zxx}, consistent with the symmetry constraints in Table I.

Appendix C: Details of First-principles calculations—The full (scalar)-relativity electronic structures of BiF_3 are calculated using density-functional theory within the pseudopotential framework. The projected augmented wave method, implemented in the Vienna *ab initio* simulation package [99–101], is employed for these calculations with the Perdew-Burke-Ernzerhof parametrization of the generalized gradient approximation exchange-correlation functional [102]. The electron wave function is expanded on a $6 \times 6 \times 1$ $\mathbf{k}$-mesh through the self-consistent computation until the energy difference is less than 10^{-6} eV. A cutoff energy of 400 eV is used for the plane-wave basis set.

To evaluate the quantum Christoffel nonlinear magnetization on a dense $\mathbf{k}$ mesh, we employ the Wannier interpolation scheme [103] implemented in the WannierBerri code package [104]. The corresponding Wannier functions are constructed using the Wannier90 code package [105], starting from the atom-centered s and p orbitals of Bi and p orbitals of F. The frozen window ranges from 0 eV to −6 eV are referenced to the Fermi energy. The nonlinear magnetization coefficient, optical conductivity, and orbital magnetic

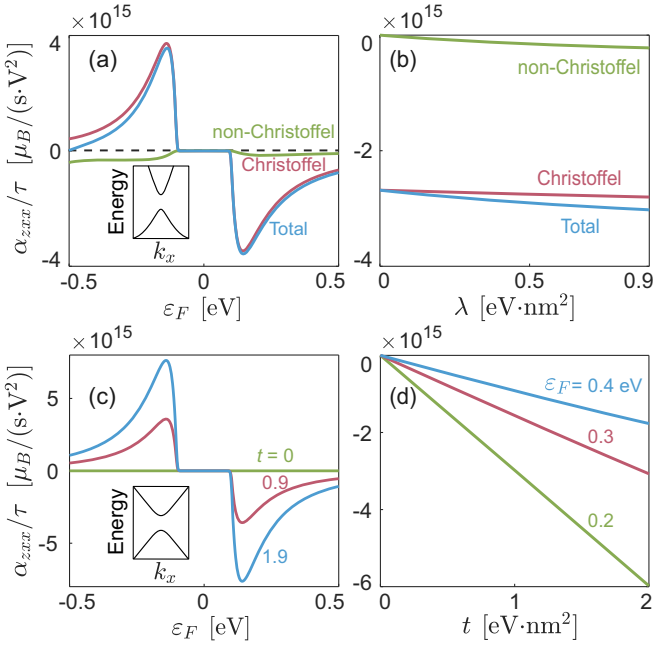

FIG. 3. Nonlinear magnetization coefficient α_{zxx} for the effective model [Eq. (B1)]. (a) α_{zxx} as a function of the Fermi energy ε_F without particle-hole symmetry ($\lambda = 0.5$ eV nm^2), for the contribution from the quantum Christoffel nonlinear magnetization and non-Christoffel contribution. (b) α_{zxx} as a function of the particle-hole symmetry breaking parameter λ at $\varepsilon_F = 0.2$ eV and $t = 0.9$ eV nm^2. (c) α_{zxx} as a function of ε_F for the particle-hole symmetric case ($\lambda = 0$) at several values of t, which breaks the $\mathcal{C}_{x,y}^2$ rotational and $\mathcal{M}_{x,y}$ mirror reflection symmetries. (d) α_{zxx} as a function of t at $\lambda = 0$ and $\varepsilon_F = 0.2$, 0.3, and 0.4 eV. Insets in (a) and (c) compare the band structures without and with particle-hole symmetry, respectively. Other model parameters are $v = 1$ eV · nm and $m = 0.1$ eV.

moment of the unit cell are evaluated on a $600 \times 600 \times 1$ **k**-mesh using the symmetrized Wannier Hamiltonian, with ten adopted refinement iterations [104].

In the simulation of nonlinear magnetization coefficient, the tetrahedron method [106,107] is employed to accurately describe the distribution function f_0' at zero temperature. In the simulation of optical conductivity, $T = 100$ K is used in the Fermi-Dirac distribution function f_0, and $\eta = 0.05$ eV is chosen in Eq. (11) to smooth the data curve.